



The Luminosity Function of Bright QSOs at $z \sim 4$ and Implications for the Cosmic Ionizing Background

Konstantina Boutsia¹, Andrea Grazian², Fabio Fontanot^{3,4}, Emanuele Giallongo⁵, Nicola Menci⁵,
Giorgio Calderone³, Stefano Cristiani^{3,4,6}, Valentina D’Odorico^{3,4,7}, Guido Cupani^{3,4}, Francesco Guarneri^{3,8}, and
Alessandro Omizzolo^{2,9}

¹ Las Campanas Observatory, Carnegie Observatories, Colina El Pino, Casilla 601, La Serena, Chile; kboutsia@carnegiescience.edu

² INAF—Osservatorio Astronomico di Padova, Vicolo dell’Osservatorio 5, I-35122, Padova, Italy

³ INAF—Osservatorio Astronomico di Trieste, Via G.B. Tiepolo, 11, I-34143 Trieste, Italy

⁴ IFPU—Institute for Fundamental Physics of the Universe, via Beirut 2, I-34151 Trieste, Italy

⁵ INAF—Osservatorio Astronomico di Roma, Via Frascati 33, I-00078, Monte Porzio Catone, Italy

⁶ INFN—National Institute for Nuclear Physics, via Valerio 2, I-34127 Trieste, Italy

⁷ Scuola Normale Superiore, P.zza dei Cavalieri, I-56126 Pisa, Italy

⁸ Dipartimento di Fisica, Sezione di Astronomia, Università di Trieste, via G.B. Tiepolo 11, I-34131, Trieste, Italy

⁹ Specola Vaticana, Vatican Observatory, 00122, Vatican City State

Received 2020 November 16; revised 2021 March 8; accepted 2021 March 9; published 2021 May 11

Abstract

Based on results by recent surveys, the number of bright quasars at redshifts $z > 3$ is being constantly revised upward. The current consensus is that at bright magnitudes ($M_{1450} \leq -27$) the number densities of such sources could have been underestimated by a factor of 30%–40%. In the framework of the QUBRICS survey, we identified 58 bright QSOs at $3.6 \leq z \leq 4.2$, with magnitudes $i_{\text{psf}} \leq 18$, in an area of 12400 deg^2 . The uniqueness of our survey is underlined by the fact that it allows us, for the first time, to extend the sampled absolute magnitude range up to $M_{1450} = -29.5$. We derived a bright-end slope of $\beta = -4.025$ and a space density at $\langle M_{1450} \rangle = -28.75$ of $2.61 \times 10^{-10} \text{ Mpc}^{-3}$ comoving, after taking into account the estimated incompleteness of our observations. Taking into account the results of fainter surveys, active galactic nuclei (AGNs) brighter than $M_{1450} = -23$ could produce at least half of the ionizing emissivity at $z \sim 4$. Considering a mean escape fraction of 0.7 for the QSO and AGN population, combined with a mean free path of 41.3 proper Mpc at $z = 3.9$, we derive a photoionization rate of $\text{Log}(\Gamma[\text{s}^{-1}]) = -12.17^{+0.13}_{-0.07}$, produced by AGNs at $M_{1450} < -18$, that is, $\sim 100\%$ of the measured ionizing background at $z \sim 4$.

Unified Astronomy Thesaurus concepts: [Quasars \(1319\)](#); [Surveys \(1671\)](#); [Cosmology \(343\)](#)

1. Introduction

Studying the quasar (QSO) and active galactic nuclei (AGNs) populations at high z is extremely important for a number of reasons. Primarily, a quantitative estimate of their space density at different luminosities can give constraints on theoretical models aiming to predict the formation and evolution of supermassive black holes (SMBHs) in the distant past (Volonteri et al. 2020). A detailed census of AGNs, both at bright and faint magnitudes at $z > 3$, can give interesting constraints on the sources responsible for the cosmological reionization of neutral hydrogen (Giallongo et al. 2015, 2019) and singly ionized helium (Worseck et al. 2019). In addition, the study of absorbers along the line of sight to bright QSOs at high z can give precise information on the physical properties of the intergalactic medium (IGM, see references in Calderone et al. 2019). Moreover, the SMBHs, ubiquitous at the center of galaxies with bulges, could be responsible, during their active phase, for the strong negative feedback that is able to suppress the star formation, eventually quenching the galaxy itself (e.g., Fiore et al. 2017) and enriching with metals the circumgalactic medium (Travascio et al. 2020). Last but not least, QSOs and AGNs in general give a major contribution to the cosmic X-ray background and an important, although probably not dominant, contribution to the infrared (IR) background (Shen et al. 2020).

One of the most studied and important observational indicators for the evolution of the AGN population is the QSO luminosity function (LF), that is, their space density as a

function of luminosity and redshift $\Phi(L, z)$. In the past, the hunt for high- z QSOs has been limited to bright magnitudes and selected areas of the sky, mainly based on photographic plates in the optical (Schmidt & Green 1983; Koo & Kron 1988) or X-ray (Boyle et al. 1993) and radio (Gregg et al. 1996). The advent of wide-area CCD detectors on dedicated 2–4 m class telescopes, that is, the Sloan telescopes, at the turn of the millennium (Fan & SDSS Collaboration 2000) has allowed the massive search for high- z QSOs at relatively bright ($i \leq 21$) optical magnitudes, breaking the record barrier of $z = 6$ with a large sample of new QSOs (Fan et al. 2006). At the present time, IR detectors allow the extension of the search for the most distant and luminous QSOs at $z > 7$ (e.g., Bañados et al. 2018; Wang et al. 2018; Yang et al. 2020).

At bright magnitudes ($M_{1450} \leq -26$), the Sloan Digital Sky Survey (SDSS) survey constituted an unprecedented milestone for the space density of bright QSOs at $z \geq 3$ for at least 20 yr, thanks to the thousands of newly discovered QSOs at high z (Lyke et al. 2020). Most of the first studies on the AGN populations at high z have been based on SDSS. Results based on these first studies remained unchallenged until the Extremely Luminous QSO Survey (ELQS, Schindler et al. 2019a, 2019b, 2017). In this survey a combination of optical and IR colors has been used to select QSOs candidates through a supervised machine-learning algorithm. This resulted in high completeness in bright magnitudes and an increase by 36% of the known QSO population in the targeted redshift range ($2.8 \leq z \leq 4.5$). This suggests that the SDSS space densities at

$z > 3.5$ and magnitudes brighter than $M_{1450} = -27$ could be underestimated by a factor of 30%–40%.

The ELQS covers the entire Northern Hemisphere and extends to slightly negative decl., but it does not cover the entire Southern sky, where major observational facilities will be deployed in the future, for example, the Extremely Large Telescope, the Square Kilometer Array, a site of the Cerenkov Telescope Array. A dedicated effort to fill this gap has been undertaken recently. A survey searching for the brightest QSOs in the Southern Hemisphere, dubbed QUBRICS (QUasars as BRiGht beacons for Cosmology in the Southern Hemisphere), produced a new sample of hundreds of QSOs at very bright optical magnitudes at $z > 2.5$ (Calderone et al. 2019; Boutsia et al. 2020).

The study of the LF of high- z AGNs is a highly debated topic. Current efforts are focused on constraining the QSO LF at $z > 6$ (Jiang et al. 2016; Matsuoka et al. 2019; Yang et al. 2019) and even close to $z \sim 8$ (Morishita et al. 2020), while the LF at $3 < z < 5$ is not settled yet, both at the bright and faint end (Shen et al. 2020). One of the major problems in the study of high- z QSOs is the completeness level of the different surveys, which is quite difficult to measure. Efficient selections of high- z QSOs (e.g., SDSS) are not usually associated with a high completeness level, as shown by Schindler et al. (2019a, 2019b). The QUBRICS survey is an attempt to search for the brightest QSOs with negative decl. with a well-defined selection criterion, which is highly complete for relatively bright objects (Boutsia et al. 2020). In this paper we consider the first subset of QSOs at $3.6 < z < 4.2$, from this survey, to study the LF of QSOs at very bright UV magnitudes $M_{1450} \sim -29$, which require wide areas on the sky and are still not well studied. In addition, we focus on regions of the sky that have been unexplored by previous studies so far, including SDSS.

In Sections 2 and 3 we present the selection procedure of the sources and the method used for calculating the LF. In Section 4 we present the best-fit parameters and discuss the contribution of the QSOs to the ionizing background based on our results. In Section 5 we compare the observed space density of $z \sim 4$ AGN with the predictions from theoretical models, and finally in Section 6 there is a summary of our results. Throughout the paper we adopt the Λ cold dark matter concordance cosmological model ($H_0 = 70 \text{ km s}^{-1} \text{ Mpc}^{-1}$, $\Omega_M = 0.3$, and $\Omega_\Lambda = 0.7$). All magnitudes are in the AB system.

2. Data

2.1. QSO Selection

In 2018 our team started the QUBRICS survey (Calderone et al. 2019). With the goal of selecting high- z QSOs candidates, we used publicly available data from several databases: (1) SkyMapper (DR1.1, Wolf et al. 2018); (2) Gaia (DR2, Gaia Collaboration et al. 2018); (3) 2MASS (Skrutskie et al. 2006); and (4) the WISE survey (Wright et al. 2010). We limited our magnitudes to the range between $14 \leq m_i \leq 18$ in order to select only bright sources and the decl. to $d < 0^\circ$ so that our sources are in the Southern Hemisphere. Then a canonical correlation analysis (CCA, Anderson 2003) was applied in order to select robust high-redshift and bright QSO candidates. This was accomplished by training the algorithm using all previously known sources with secure identification from the literature.

The recipe obtained through CCA training has been applied to the rest of the sample in order to predict a classification. Stars have been identified based on parallax and proper motion information by Gaia and make up for $\sim 83\%$ of the sample. For sources classified as QSOs, a redshift estimate has been obtained using the CCA as a regression algorithm. This allowed us to reject lower-redshift QSOs ($z < 2.5$). The final list of high-redshift bright QSOs included 1412 candidates. A pilot survey led to the initial discovery of 54 QSOs with $z \geq 2.5$. For more details about the selection method please refer to Calderone et al. (2019) (hereafter Paper I).

2.2. Spectroscopic Followup

Based on the encouraging results of the QUBRICS pilot campaign, we have undertaken a more systematic spectroscopic follow-up for confirming the nature of more candidates. We have been awarded time at several facilities including the Low Dispersion Survey Spectrograph (LDSS-3) at the Clay Magellan telescope, the Inamori Magellan Areal Camera and Spectrograph (IMACS) at the Baade Magellan telescope, the Wide Field CCD (WFCCD) at the duPont telescope, and the ESO Faint Object Spectrograph and Camera (EFOSC2) at the New Technology Telescope (NTT). We observed 511 sources, managing to obtain secure classification and redshift determination for 432. Most of our confirmed sources ($\sim 52\%$) were bright QSOs at $z \geq 2.5$, of which 15 were at a redshift $z > 4$. Our main contaminants were lower-redshift QSOs or AGN ($z < 2.5$, $\sim 38\%$), while the rest were galaxies and stars ($\sim 10\%$).

Taking into consideration the results of this campaign, we have updated the training sample and rerun the classification algorithm, thus obtaining a more robust list of candidates. In fact, based on this self-learning approach, our completeness has improved and is currently $> 90\%$, while the success rate is close to 70%. More details about the results of the spectroscopic follow-up can be found in Boutsia et al. (2020) (hereafter Paper II). The current sample of QSO candidates, in the redshift range $3.6 < z < 4.2$, is based on the most recent selection described in Paper II.

In the period 2020 November–2021 January and after the publication of Paper II, we continued the spectroscopic follow-up of our $3.6 < z_{\text{cca}} < 4.2$ QSO candidates. Observations have been obtained with IMACS and LDSS-3 at the Magellan telescopes. On LDSS-3 we used the $1''$ -center slit with the VPH-all grism and no filter. This results in a wavelength coverage of 4000–10000 Å at an $R \sim 900$ resolution. In order to obtain a similar resolution with IMACS we used the #300 grism at a blaze angle of $17^\circ 5$ and the $1''$ slit covering a wavelength range of 4000–10000 Å. The data reduction and calibration for both instruments have been done following the recipes presented in Paper II. The sources presented for the first time in this work are commented on in Table 1 as “new data.” Currently, from our initial candidate sample with $3.6 < z_{\text{cca}} < 4.2$, only 15 sources remain without spectroscopic follow-up, of which 2–3 are of high quality. Thus our sample can be considered spectroscopically complete.

3. Analysis and Methods

Table 1 contains the 58 QSOs of $3.6 \leq z_{\text{spec}} \leq 4.2$ and $i_{\text{psf}} \leq 18.0$ in the QUBRICS footprint.

Table 1
The $3.6 \leq z_{\text{spec}} \leq 4.2$ QSOs at $i_{\text{psf}} \leq 18.0$ in the QUBRICS Survey

$ID_{\text{Skymapper}}$ DR1.1	R.A. J2000	Decl. J2000	z_{spec}	i_{psf} AB	M_{1450}	Reference
68291629	11:35:36.40	+08:42:19.08	3.847	17.966	-27.915	DR14 ^a
65558414	12:49:57.26	-01:59:28.76	3.665	17.960	-27.809	ELQS ^b
57913424	11:49:14.40	-15:30:43.97	4.129	17.756	-28.289	Paper I
65911949	13:20:29.98	-05:23:35.29	3.700	17.444	-28.346	Mitchell et al. (1990)
56483517	09:35:42.70	-06:51:18.93	4.040	17.424	-28.570	PSELQS ^c
113197224	16:16:48.96	-09:14:44.39	4.055	17.876	-28.126	PSELQS
114286192	16:21:16.93	-00:42:50.87	3.703	17.386	-28.405	ELQS
10623942	03:05:17.92	-20:56:28.12	3.960	17.960	-27.988	PSELQS
68092164	11:30:10.59	+04:11:28.12	3.930	17.718	-28.212	Schneider et al. (2005)
56662952	09:40:24.13	-03:23:04.07	3.900	17.630	-28.282	PSELQS
58206167	10:14:30.28	-04:21:40.31	3.890	17.571	-28.336	Paper I
57936842	10:20:00.81	-12:11:51.49	3.715	17.904	-27.897	PSELQS
98382043	15:23:12.41	-16:27:22.92	4.120	17.977	-28.063	PSELQS
13303827	04:11:02.07	-01:35:15.10	3.660	17.911	-27.854	PSELQS
135386798	20:03:24.11	-32:51:45.05	3.783	17.296	-28.545	Peterson et al. (1982)
7766951	01:03:05.51	-24:49:25.20	3.865	17.758	-28.135	PSELQS
7437380	00:03:22.95	-26:03:18.17	4.111	17.071	-28.963	Sargent et al. (1989)
5533851	23:09:59.27	-12:26:02.91	3.730	17.863	-27.946	PSELQS
8489172	01:13:51.96	-09:35:51.17	3.668	17.875	-27.895	DR14
9182350	02:16:46.94	-09:21:07.21	3.675	17.762	-28.013	DR14
10165846	01:50:48.82	+00:41:26.31	3.703	17.970	-27.821	Trump et al. (2006)
8566706	01:40:49.17	-08:39:42.40	3.713	17.635	-28.163	ELQS
8937029	02:21:23.90	-14:16:54.87	3.650	17.753	-28.005	PSELQS
8430815	01:03:18.06	-13:05:09.89	4.072	17.242	-28.770	Paper II
136588662	20:11:58.77	-26:23:40.86	3.657	17.662	-28.102	Paper II
58181076	10:51:22.70	-06:50:47.82	3.810	17.345	-28.513	Paper II
57143774	10:52:21.62	-19:52:37.95	3.660	17.741	-28.024	Paper I
57929040	10:15:29.37	-12:13:14.23	4.190	17.255	-28.824	Paper I
10739949	04:07:45.29	-32:15:37.84	3.750	17.693	-28.128	Paper I
10934139	04:50:11.37	-43:24:29.75	3.946	17.798	-28.142	Paper I
57933437	10:15:44.12	-11:09:22.80	3.865	17.485	-28.408	Paper I
302866544	19:18:57.68	-65:44:52.38	3.842	17.848	-28.029	Paper I
135100950	19:53:02.67	-38:15:48.40	3.712	17.305	-28.492	Paper I
136198132	20:17:41.49	-28:16:29.83	3.685	17.388	-28.394	Paper I
2379862	21:25:40.96	-17:19:51.32	3.897	16.548	-29.363	Paper I
57368436	10:54:49.69	-17:11:07.36	3.750	17.107	-28.714	Paper I
5528935	23:08:27.03	-13:32:56.21	3.830	17.736	-28.134	PSELQS
317253125	00:48:05.34	-59:29:09.44	3.607	17.536	-28.196	Paper II
317343050	01:27:16.87	-58:02:47.28	3.918	17.772	-28.152	Paper II
58723356	11:13:32.47	-03:09:13.98	3.731	17.949	-27.860	Paper II
315607762	03:17:24.89	-57:36:19.01	3.844	17.922	-27.956	Paper II
310206031	05:09:43.13	-74:09:47.89	3.773	17.575	-28.260	Paper II
316591563	05:29:14.28	-45:08:07.03	3.690	17.661	-28.123	Paper II
14930439	04:36:23.92	-00:04:02.89	3.852	17.404	-28.479	Paper II
305336573	21:08:17.67	-62:17:57.53	3.794	17.589	-28.259	Paper II
317411112	00:18:30.46	-53:35:35.20	3.738	17.744	-28.070	Paper II
316292063	05:48:03.20	-48:48:13.19	4.147	16.886	-29.169	Paper II
307536920	21:51:37.44	-44:36:44.17	3.638	17.363	-28.388	Paper II
6932623	02:04:13.26	-32:51:22.80	3.835	17.068	-28.807	Paper II
8789744	01:55:58.27	-19:28:48.98	3.655	17.393	-28.370	Paper II
4045023	21:55:13.29	-03:16:05.61	3.690	17.410	-28.374	Paper II
6986244	02:35:57.55	-34:48:56.45	3.737	17.792	-28.022	new data
10444829	04:08:28.43	-39:00:32.93	3.610	17.817	-27.916	new data
10331020	03:12:52.40	-31:38:33.21	3.879	17.828	-28.072	new data
309271177	02:10:51.46	-84:54:37.57	3.685	17.170	-28.609	new data
305864039	23:34:54.76	-69:30:42.84	3.894	17.856	-28.052	new data
316874745	03:27:24.51	-52:38:58.20	3.771	17.787	-28.047	new data
60628332	12:11:20.09	-33:14:27.46	3.826	17.728	-28.141	new data

Notes. QSOs with $M_{1450} > -28.0$ are not used for the LF calculations.

^a DR14 refers to Pâris et al. (2018).

^b ELQS refers to Schindler et al. (2019b).

^c PSELQS refers to Schindler et al. (2019a).

The ELQS survey by Schindler et al. (2019a, 2019b) includes other QSOs in the same redshift and magnitude interval, falling in the QUBRICS area but not listed in Table 1. The main reason is that those QSOs have magnitudes $i_{\text{psf}} > 18.0$ in Skymapper DR1.1, while the i -band magnitudes by Schindler et al. (2019a, 2019b) have been drawn from SDSS and Pan-STARRS1 (PS1, Chambers et al. 2016) photometry.

The QSO 015041-250846 by Schindler et al. (2019a) at $z = 3.600$ (id = 7250804) is not included in our sample since, based on our data, we calculated a spectroscopic redshift of $z = 3.596$ (Paper II). This is slightly lower than our redshift cut for the LF calculations.

Three QSOs from the literature, 58209836 and 58674889 from Schindler et al. (2019b) and BRI 1117-1329 from Storrie-Lombardi et al. (1996), were not part of our sample, due to incomplete photometry in the Skymapper and WISE databases. We checked a posteriori that they have $i_{\text{psf}} \leq 18.0$ and fall on the QUBRICS footprint, so in principle, we should include them in our sample. In practice, we decided to compute the LF of $z \sim 4$ AGN by using only objects from our main sample, with the appropriate completeness corrections. The result would have been approximately the same if we had included them in our calculations but had neglected the incompleteness correction. Thus, only the sources presented in Table 1 were used to compute the LF of QSOs at $3.6 \leq z_{\text{spec}} \leq 4.2$ at the bright end, that is, $M_{1450} \leq -28.0$.

Absolute magnitudes at 1450 Å rest frame (M_{1450}) in Table 1 have been derived from the apparent magnitudes i_{psf} of Skymapper and from the spectroscopic redshifts with the equation

$$M_{1450} = i_{\text{psf}} - 5 \log(d_L) + 5 + 2.5 \log(1 + z_{\text{spec}}) + K_{\text{corr}}, \quad (1)$$

where d_L is the luminosity distance in parsec (pc) and the k correction K_{corr} is given by the expression

$$K_{\text{corr}} = -2.5 \alpha_\nu \log_{10}(\lambda_{\text{obs}} / (1 + z_{\text{spec}}) / \lambda_{\text{rest}}), \quad (2)$$

where $\alpha_\nu = -0.7$ is the typical spectral slope of QSOs, $\lambda_{\text{rest}} = 1450 \text{ \AA}$, and $\lambda_{\text{obs}} = 7799 \text{ \AA}$ is the central wavelength of the i_{psf} filter.

3.1. Completeness Corrections

Correcting the AGN space density for possible incompleteness effects is important for the comparison of the QUBRICS LF with the results of other surveys. The completeness of the QUBRICS sample at $3.6 < z_{\text{spec}} < 4.2$ has three factors:

1. c1: Sources that are not part of the main sample of 1014875 objects, which is the starting catalog of QUBRICS, as described in Papers I and II.
2. c2: Sources that are part of the main sample but have not been selected by the CCA or z_{CCA} criteria of Paper I or Paper II.
3. c3: QSO candidates that are still missing spectroscopic identification.

In our analysis, we can assume that $c2 = 1.0$, since in Table 1 we provide all the confirmed QSOs that are part of the main sample, regardless of whether they have been selected by the criteria of Papers I, II, or other surveys. This choice has been achieved in order to be less dependent on the assumptions usually carried out in completeness simulations, for example,

the QSO spectral slopes, the equivalent width distribution of the emission lines, the IGM transmission, or the photometric noise of the employed catalogs.

Regarding the correction factor $c3$, only 15 QSO candidates with $3.6 < z_{\text{CCA}} < 4.2$ are still missing spectroscopic identification, but among them, we expect to find no new QSOs at $z \sim 4$: indeed, after visual inspection of their spectral energy distributions, we have preliminary indications that they are probably not high- z QSOs. Only two sources have a spectral energy distribution consistent with $z \sim 4$ QSOs. Thus we can safely assume here that $c3 = 1.0$, with small uncertainties with respect to the measured Poissonian errors of our sample.

Estimating the correction factor $c1$ is not an easy task. With this aim, we start our analysis from 881 known QSOs with $3.6 < z_{\text{spec}} < 4.2$ used in Paper I as a training set for our CCA selection. In this case, we do not introduce the new QSOs discovered by QUBRICS in this analysis. We cross-correlate these 881 QSOs with the public catalog of Gaia EDR3 (Gaia Collaboration et al. 2021), restricting the analysis to the area covered by QUBRICS and limiting the R_p magnitude of Gaia at $R_p^{\text{Gaia}} \leq 17.67$, which corresponds to a Skymapper i -band magnitude $i \leq 18.0$, which is the main criterion for our main sample. We verify that the adopted photometric cut is consistent with a selection in absolute magnitudes M_{1450} brighter than -28.0 , which is the fainter limit of our LF. We end up with 32 known QSOs with $3.6 < z_{\text{spec}} < 4.2$. We then cross-correlate these 32 objects with our main sample, finding 27 sources. The five missing objects are bright ($i < 18.0$) QSOs, but they have not been selected in our main sample, due to their photometric flags in Skymapper or WISE surveys. Considering these numbers ($27/32 = 0.844$), the correction factor $c1$ is 1.185 ($1/0.844$), and it does not depend on the Skymapper i -band magnitudes of the selected QSOs.

Summarizing, we have applied a correction factor of 1.185 to the space density of $z \sim 4$ QSOs of QUBRICS shown in Figure 1. The absolute magnitude versus redshift of all known QSOs with $M_{1450} < -27$ are shown in Figure 2. Only sources that are part of the main sample and have an absolute magnitude of $M_{1450} < -28$ (red and cyan points) have been used to calculate the LF.

4. Results: QSO Density Determination

The space density of bright QSOs at $z \sim 4$ has been derived by adopting the $1/V_{\text{max}}$ approach (Eales 1993), where the accessible volume for each object has been computed from the redshift interval encompassing $3.6 \leq z \leq 4.2$ and the magnitude limits of the survey. The accessible volume has been corrected by the factor 1.185 due to possible incompleteness of our survey, as discussed in the previous section.

The total area of the QUBRICS survey adopted here is 12400 deg^2 , and the sample is limited to $14.0 \leq i_{\text{psf}} \leq 18.0$ (Papers I and II). Only robustly confirmed QSOs (i.e., flagA) in the redshift interval $3.6 \leq z \leq 4.2$ have been used in the LF calculation. Error bars to the QSO space density have been computed by adopting the statistics of Gehrels (1986), which are particularly suited for low number counts, while they are close to Poisson for large numbers.

We set the faintest absolute magnitude limit for the LF estimate to $M_{1450} = -28.0$, which is the luminosity of an object at $i_{\text{psf}} = 18.0$ at $z = 4.2$, at the redshift limit of our survey. This criterion includes 47 out of 58 sources presented in Table 1. We compute the QSO space density in three independent

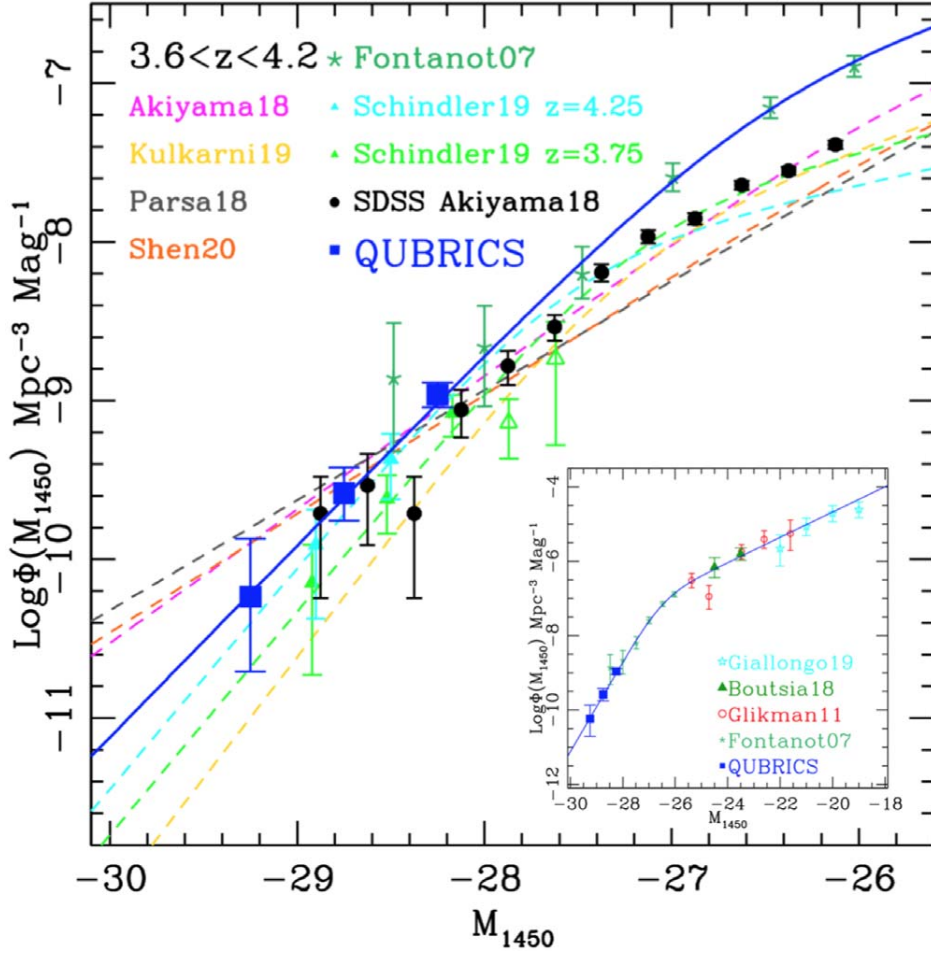


Figure 1. The LFs of QSOs at $3.6 \leq z \leq 4.2$ from QUBRICS (blue filled squares) compared to other LFs from the recent literature. All the data points and curves have been shifted to $z = 3.9$ adopting the density evolution recipe by Schindler et al. (2019b) with $\gamma = -0.38$. The best-fit result is shown by the blue line. In the bottom-right inserted plot we show the best-fit LF extended to faint magnitudes, as discussed in Section 4.1

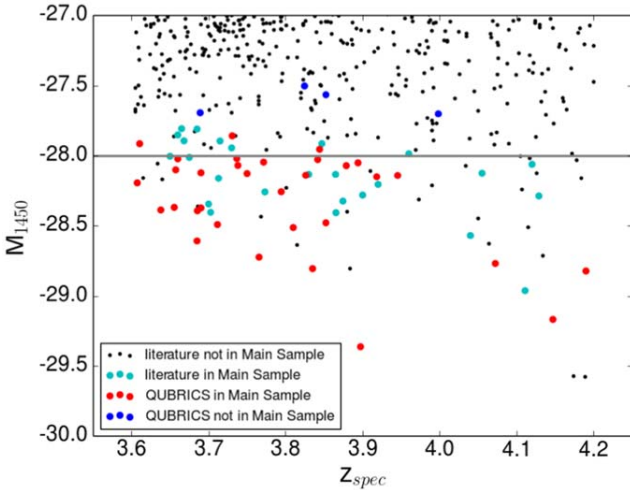


Figure 2. Absolute magnitude M_{1450} vs. spectroscopic redshift for all known QSOs in the redshift range $3.6 \leq z_{\text{spec}} \leq 4.2$. Red symbols show the sources observed by QUBRICS and are part of the main sample. Blue symbols are sources observed by QUBRICS but are not part of the main sample. Cyan points show QSOs known from the literature that are also part of the main sample. Sources with $M_{1450} \leq -28$ that are also part of the main sample (red and cyan points) have been used for calculating the LF function in this work. The line indicates the $M_{1450} = -28$ magnitude limit.

intervals of absolute magnitudes, from the brightest limit $M_{1450} = -29.5$ to $M_{1450} = -28.0$. In Figure 1 we show the three independent bins. Table 2 summarizes the observed space densities of bright QSOs found by QUBRICS in the redshift interval $3.6 \leq z \leq 4.2$.

A first consideration drawn from Figure 1 is that the bright end of the LF at $z \sim 4$ is rather steep, if compared with previous results by SDSS (e.g., Fan et al. 2001; Richards et al. 2003) as well as recent results (Akiyama et al. 2018; Shen et al. 2020).

We have carried out a maximum likelihood analysis of the $z \sim 4$ QUBRICS QSOs following the formalism by Marshall et al. (1983). We have fitted a single power law with slope β , finding a best-fit value of $\beta = -4.14$ with a 68% confidence level interval between -4.87 and -3.56 . This confirms the previous result of the ELQS survey by Schindler et al. (2019b) of a relatively steep slope of the bright end of the $z = 4$ QSO LF.

An attempt to fit the LF with a double power law has shown strong degeneracies between the bright-end slope β and M^* (the absolute magnitude of the LF knee). This is expected since from previous work (McGreer et al. 2013; Schindler et al. 2019b) it is known that this parameter is $M^* \sim -26$ at $z \sim 3-4$, much fainter than our survey limit. Using the QUBRICS sample presented in this paper, we are only able to put 1σ constraints of $\beta < -3.33$ and $M^* > -29.10$. This is somehow

Table 2
The Space Density Φ of $3.6 \leq z \leq 4.2$ QSOs in the QUBRICS Footprint

Interval	$\langle M_{1450} \rangle$	N_{QSO}	Φ cMpc $^{-3}$	$\sigma_{\Phi}(\text{up})$ cMpc $^{-3}$	$\sigma_{\Phi}(\text{low})$ cMpc $^{-3}$
$-28.5 \leq M_{1450} \leq -28.0$	-28.25	36	1.089E-09	2.136E-10	1.809E-10
$-29.0 \leq M_{1450} \leq -28.5$	-28.75	9	2.611E-10	1.196E-10	8.581E-11
$-29.5 \leq M_{1450} \leq -29.0$	-29.25	2	5.802E-11	7.712E-11	3.838E-11

Note. The space density Φ has been corrected for incompleteness, as discussed in the main text.

expected given that our survey is limited to $M_{1450} = -28.0$, much brighter than the expected break of the LF of $z \sim 4$ QSOs. For these reasons, we decided to add fainter space densities from the literature in order to provide a best-fit analysis of all the parameters (α , β , M^* , Φ^*) of the QSO LF, as we describe in the following section.

Another notable point of Figure 1 is the QSO space density at $M_{1450} = -29.25$, which is a unique determination not available in other surveys. This confirms the unique added value of the QUBRICS survey and its success in finding the most rare and brightest cosmic beacons, at least in the Southern Hemisphere.

Our LF determination is in agreement with the brightest points of SDSS (Akiyama et al. 2018) and with Schindler et al. (2019b) at $z = 4.25$. The error bars of our data points are significantly smaller than the SDSS and the ones presented by Schindler et al. (2019a, 2019b). Results from Schindler et al. (2019a) indicate that SDSS can be incomplete at the $\sim 40\%$ level, confirming previous values by Fontanot et al. (2007). The results of the QUBRICS survey, shown in Figure 1, seem to confirm such statements.

4.1. Best Fit to LF Data Down to $M_{1450} = -18$

In order to provide a best fit to the QUBRICS data on a wider magnitude range that covers both the bright and faint ends, we also considered LF determinations at lower luminosities. For this analysis, we adopted a double power-law function for the LF as described below:

$$\phi = \frac{\phi^*}{10^{0.4(M - M_{1450}^*)(\alpha + 1)} + 10^{0.4(M - M_{1450}^*)(\beta + 1)}}. \quad (3)$$

We include in our best-fit analysis the data from Fontanot et al. (2007, hereafter F07), based on a reanalysis of the SDSS survey at $z \sim 4$ with a revised selection function. The refined completeness correction by F07 induces a steep space density of QSOs at $M_{1450} \sim -26$, which is higher than the one computed by Akiyama et al. (2018) (but consistent to a 1σ level up to $M_{1450} \sim -28$).

We decided not to use the Akiyama et al. (2018) QSO LF in this work since we have indications from other works that it could be underestimated. In Boutsia et al. (2018), for example, it is shown that the AGN space density of Akiyama et al. (2018) is three times lower than the one in the COSMOS field at $M_{1450} \sim -23$ and five times lower than the estimates by Glikman et al. (2011) on the NDWFS and DLS fields, as also discussed in Giallongo et al. (2019). Boutsia et al. (2018) have also shown that this discrepancy cannot be due to cosmic variance effects on the COSMOS, NDWFS, or DLS areas. Since the Fontanot et al. (2007) LF is in better agreement with the results of Glikman et al. (2011) and Boutsia et al. (2018),

Table 3

The Best-Fit Parameters of the QSO LF at $3.6 \leq z \leq 4.2$ in the QUBRICS Footprint

α	β	M_{1450}^*	$\text{Log}\Phi^*$
$-1.850^{+0.150}_{-0.250}$	$-4.025^{+0.575}_{-0.425}$	$-26.50^{+0.85}_{-0.60}$	$-6.85^{+0.60}_{-0.45}$

Note. The errors associated with the best-fit parameters are at the 68% confidence level (1σ).

both of which have been based on spectroscopically complete samples of $z \sim 4$ AGN, we decided to adopt for our purpose the F07 QSO LF, which covers the range of absolute magnitudes $-28 < M_{1450} < -24$.

Going at fainter luminosities, we rely on the results by Glikman et al. (2011), Boutsia et al. (2018), and Giallongo et al. (2019). The best fit of the LF has been carried out by a minimum χ^2 analysis on the abovementioned binned data points. The best-fit result is shown in the bottom-right inserted plot in Figure 1, and the best-fit parameters, together with their 1σ uncertainty ranges are summarized in Table 3.

At bright magnitudes, space densities are higher than previous fits by Kulkarni et al. (2019) and Schindler et al. (2019b) at $z = 3.75$; and Akiyama et al. (2018) and Shen et al. (2020) at $M \geq -28$. At fainter luminosities, the best fit by Schindler et al. (2019b) at $z = 4.25$ is also inconsistent with the observed data points of F07, and all the previous results in the literature failed to reproduce the observed data points, especially at the faint side.

Based on the updated fit provided in Figure 1, we proceed with the derivation of the ionizing background produced by bright QSOs, and faint AGNs, at $z \sim 4$.

4.2. The Ionizing Background at $z \sim 4$ Produced by QSOs and AGNs

The detailed knowledge of the QSO LF at $z \sim 4$ can be used to estimate the AGN contribution to the photon volume emissivity (\dot{N}_{ion}) and photonization rate (Γ) (Figure 3). We apply the same formalism as in Fontanot et al. (2014) and Cristiani et al. (2016):

$$\dot{N}_{\text{ion}}(z) = \int_{\nu_H}^{\nu_{\text{up}}} \frac{\rho_{\nu}}{h_p \nu} d\nu, \quad (4)$$

$$\rho_{\nu} = \int_{L_{\text{min}}}^{\infty} f_{\text{esc}}(L, z) \Phi(L, z) L_{\nu}(L) dL, \quad (5)$$

where ρ_{ν} is the monochromatic comoving luminosity density brighter than L_{min} , ν_H is the frequency corresponding to 912 Å, and $\nu_{\text{up}} = 4\nu_H$.

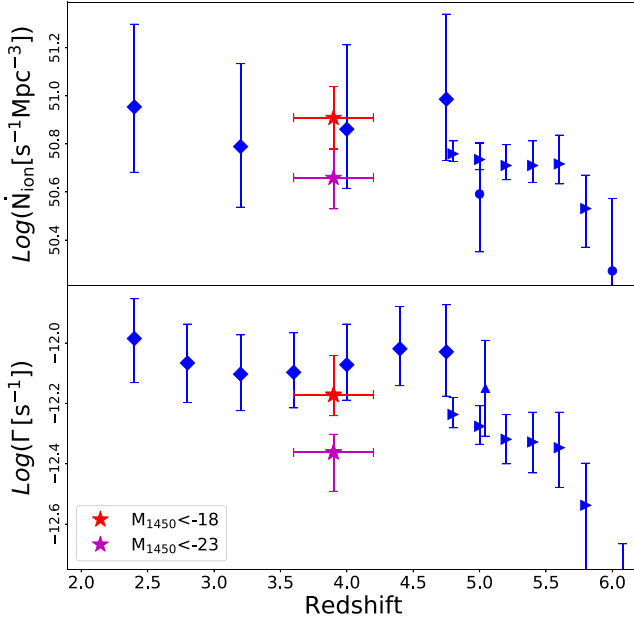


Figure 3. Contribution of the AGN population to the ionizing background (*upper panel*) and to the photoionization rate (*lower panel*), based on our LF estimate, assuming a density evolution as in Schindler et al. (2019b) and a mean escape fraction (f_{esc}) of 0.7. The magenta star shows the contribution integrating to an absolute magnitude of -23 and the red star to -18 . Error bars have been calculated as discussed in Section 4.2. Observed data are from Wyithe & Bolton (2011, circles), Becker & Bolton (2013, diamonds), and D’Aloisio et al. (2018, triangles).

The evolution of the photoionization rate Γ with redshift follows the parameterization presented by Haardt & Madau (2012):

$$\Gamma(z) = 4\pi \int_{\nu_{\text{H}}}^{\nu_{\text{up}}} \frac{J(\nu, z)}{h_p \nu} \sigma_{\text{HI}}(\nu) d\nu, \quad (6)$$

where $\sigma_{\text{HI}}(\nu)$ is the absorbing cross section for neutral hydrogen and $J(\nu, z)$ is the background intensity:

$$J(\nu, z) = c / 4\pi \int_z^{\infty} \epsilon_{\nu 1}(z_1) e^{-\tau_e} \frac{(1+z)^3}{(1+z_1)^3} \left| \frac{dt}{dz_1} \right| dz_1, \quad (7)$$

where ν_1 is the proper volume emissivity and $\tau_e(\nu, z, z_1)$ represents the effective opacity between z and z_1 . Starting from the functional form we estimate for the QSO LF at $3.6 < z < 4.2$, we assume a pure density evolution consistent with the SDSS results (Schindler et al. 2019b), a bivariate distribution of absorbers as in Becker & Bolton (2013), an escape fraction $f_{\text{esc}} = 0.7$ (Cristiani et al. 2016) for all QSOs, and a mean free path of 41.3 proper Mpc (pMpc) at $z = 3.9$ (Worseck et al. 2014). We then solve the equations of the radiative transport in a cosmological context (see e.g. Haardt & Madau 2012), assuming two different luminosity limits for the QSO LF, corresponding only to the QSO contribution ($M_{\text{UV}} < -23$) and to the total AGN population ($M_{\text{UV}} < -18$).

Following the considerations by D’Aloisio et al. (2018), we have increased the values of the ionizing emissivity by a factor of 1.2 to take into account the contribution by radiative recombination in the IGM. The resulting values are shown in Figure 3 as red and magenta stars, and we collect the values in Table 4. The reported error bars (corresponding to the 16th and 84th percentiles of the distribution) are obtained by means of

Table 4

The Photon Volume Emissivity and Photoionization Rate per Hydrogen Atom Produced by Bright QSOs and Faint AGNs at $z = 3.9$

$M_{\text{UV}}^{\text{lim}}$	$\text{Log}(N_{\text{ion}} [\text{s}^{-1} \text{Mpc}^{-3}])$			$\text{Log}(\Gamma [\text{s}^{-1}])$		
	50th	16th	84th	50th	16th	84th
-23	50.66	50.53	50.78	-12.36	-12.49	-12.30
-18	50.91	50.78	51.04	-12.17	-12.24	-12.04

$\sim 25,000$ Monte Carlo realizations varying (a) the QSO LF parameters within the 3σ confidence level defined by our minimization procedure, taking into account all relevant covariances; and (b) the intrinsic spectral slope of AGN emission between a single slope ($f_{\nu} \propto \nu^{\alpha}$ with $\alpha = -0.69$) and a broken power law (with $\alpha = -1.41$ at $\lambda < 1000 \text{ \AA}$). Our estimates are then compared with a set of observational determinations from Wyithe & Bolton (2011), Becker & Bolton (2013), and D’Aloisio et al. (2018).

Based on Figures 1 and 3 the following considerations can be drawn: (1) the statistical errors on the LF determinations at $z \sim 4$ are very small and currently no serious issue is present. It is quite implausible that in the future new surveys of QSOs and AGNs at this redshift will change this picture dramatically, considering that our survey is spectroscopically complete. (2) Uncertainties in the photoionization rate Γ are mainly due to systematic effects, more precisely, the knowledge of the escape fraction of faint AGN and of the mean free path of QSO and AGN ionizing photons at $z \sim 4$ (e.g., Romano et al. 2019). In addition, measurements of the ionizing background are still uncertain by a factor of 2 (Faucher-Giguère et al. 2008 vs. Becker & Bolton 2013). Improving such uncertainty would provide useful answers on the temperature of the IGM.

Recent predictions presented by Dayal et al. (2020) conclude that at $z = 4$ AGNs can provide a maximum of 25% to the cumulative ionizing emissivity, considering a variety of models and escape fraction values. Their contribution could go as high as 50%–83% at $z = 5$. Our observations of the photoionization rate indicate that AGN at $z = 4$ and $M_{1450} < -23$ can provide more than 50% of the UV background and an even larger fraction if a different estimate for the ionizing background, like Faucher-Giguère et al. (2008), is considered. Reaching a sound conclusion on the role of AGNs in the production of ionizing photons in the post-reionization era needs a clarification on the exact value of the ionizing background and on the mean free path of H I ionizing photons at $z \sim 4$. To a lesser extent, the measurement of the Lyman continuum (LyC) escape fraction (f_{esc}) of faint AGNs is another important unknown in the present calculations.

If the f_{esc} of faint AGNs is significantly below 70%, then the calculations above are not far from the real numbers: following Giallongo et al. (2019), AGNs fainter than -23.0 are contributing only 10%–20% to the total ionizing background produced by accreting SMBHs. The escape fraction of an AGN at $M_{1450} \leq -23$ turns out to be $\geq 70\%$ (Cristiani et al. 2016; Grazian et al. 2018), without any trend with the observed optical luminosities. If the escape fraction is rapidly dropping to zero at fainter magnitudes, then the total photoionizing background would be lower by only 20%, which is relatively small compared with the bigger uncertainties still present on other quantities (the mean free path and the UV background at present have uncertainties of the order of 50%). In the future it will be very important to derive with great accuracy the value

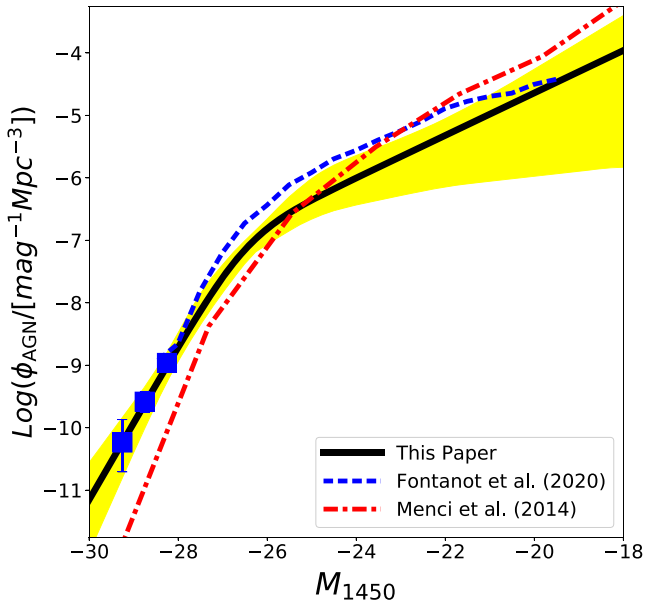


Figure 4. Comparison of our best-fit high- z LF with predictions from SAMs. The shaded area represents the 3σ uncertainty range corresponding to the best-fit parameters for the LF. Blue dashed and red dotted–dashed lines correspond to predictions from GAEA (Fontanot et al. 2020) and the Rome SAM (Menci et al. 2014), respectively.

of the ionizing background at $z \sim 4$ (Faucher-Giguère et al. 2008; Becker & Bolton 2013) and the mean free path of H I ionizing photons (Prochaska et al. 2009; Worseck et al. 2014; Romano et al. 2019). The LyC escape fraction of AGN fainter than $M_{1450} = -23$ is also important, but not as fundamental, in the derivation of an accurate measurement for the photoionizing background in the post-reionization epoch.

5. Discussion

5.1. Comparison with Theoretical Models

We can compare the estimated high- z QSO LF with the predictions of theoretical models of galaxy formation and evolution. In particular, we consider the predictions of two semianalytic models (SAMs), the GALaxy Evolution and Assembly model (GAEA, Fontanot et al. 2020) and the Rome SAM (Menci et al. 2014). These models are able to describe the formation and evolution of galaxies, starting from a statistical description of the Large Scale Structure and the distribution of the dark matter haloes and assuming prescriptions (either empirically or theoretically motivated) to describe the key physical processes acting on the baryonic component. In particular, the models we consider in Figure 4 have been calibrated to reproduce the evolution of the bolometric QSO LF as described by optical (e.g., Hopkins et al. 2007) and X-ray (e.g., Ueda et al. 2014) surveys.

Both models reproduce reasonably well our estimate of the QSO LF over the whole magnitude range (black solid line; the shaded region represents the 3σ uncertainty range), with a possible overestimate of sources at $M_{1450} > -23$. The GAEA predictions are taken from a run based on merger trees extracted from the Millennium Simulation (Springel et al. 2005). The Millennium Simulation volume is barely enough to sample the magnitudes corresponding to the fainter of our QUBRICS data (blue squares in Figure 4), whose space density is in good agreement with model predictions. On the other

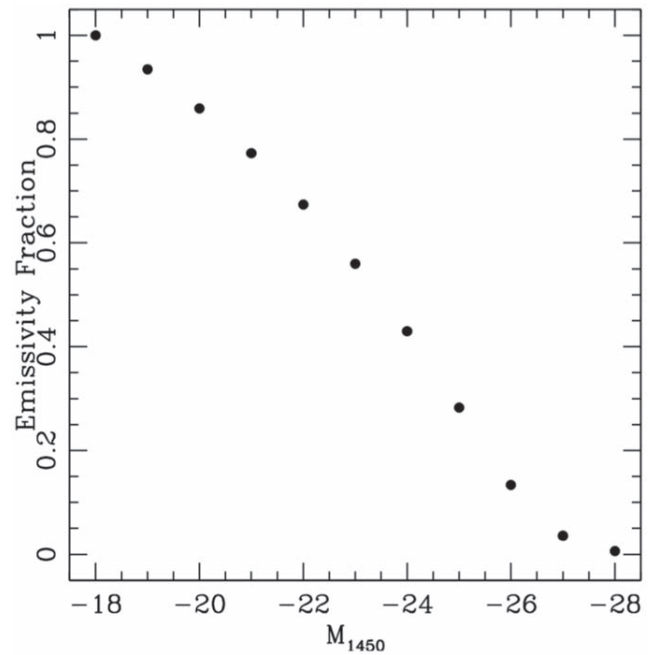


Figure 5. Fraction of integrated ionizing emissivity at $z \sim 3.9$.

hand, the Menci et al. (2014) SAM is based on merger trees following the extended Press–Schechter approach and is able to sample space densities corresponding to brighter magnitudes. The trigger for the black hole accretion is provided by the minor and major interactions, in addition to the disk instability that should be of little influence in such bright QSOs. Nonetheless, at these luminosities this model predicts space densities slightly below the QUBRICS estimate.

It is important to keep in mind that, despite the fact that these models have been explicitly calibrated to reproduce the evolution of the bolometric QSO LF, this effort typically focuses on the knee of the LF, where most of the sources lie. The bright end of the LF, on the other hand, is populated by the most extreme objects, either in terms of accretion rate or SMBH mass, and Figure 4 clearly shows the relevant degree of uncertainty in this luminosity regime. These sources are indeed the most difficult to model, although they bring a lot of information on the evolution of structures in the early stages of structure formation.

5.2. Additional Considerations

Figure 5 provides the fraction of ionizing emissivity ϵ_{912} produced by $z \sim 4$ QSOs at different luminosities. The fraction is relative to the emissivity computed for $M_{1450} \leq -18$, according to the following equations:

$$\epsilon_{\text{ion}}(z) = \langle f \rangle \epsilon_{912} \quad (8)$$

and

$$\epsilon_{912} = \int_{\phi} (L_{1450}, z) L_{1450} \left(\frac{1200}{1450} \right)^{0.44} \left(\frac{912}{1200} \right)^{1.57} dL_{1450}, \quad (9)$$

where $\langle f \rangle$ is the average escape fraction from QSOs and ϵ_{912} is the ionizing emissivity produced by QSO activity. The results are consistent with the one obtained by Giallongo et al. (2019), modulo the fact that our LF is slightly steeper, both in the bright and faint end, and that the break of our fit is located at a

slightly brighter luminosity. The main reason for these differences is that in our fit we did not consider the SDSS data by Akiyama et al. (2018), which are lower than the ones by Fontanot et al. (2007), Glikman et al. (2011), and Boutsia et al. (2018).

From Figure 5 it is easy to conclude that QSOs brighter than $M_{1450} = -23.0$ provide at least half of the ionizing emissivity at $z \sim 4$. If an escape fraction of 75% is assumed for QSOs brighter than $M_{1450} = -23.0$, and a lower escape fraction of 25% is assumed for the fainter population, then the total emissivity will result in 50.8% ($0.515 \cdot 0.75 + 0.485 \cdot 0.25 = 0.5075$). It is worth noting that for $z \sim 4$ QSOs brighter than $M_{1450} = -23.0$, the measurements of the escape fraction give values larger than 70% (Cristiani et al. 2016; Grazian et al. 2018), without any trend with the luminosity. Thus, the scenario where sources fainter than $M_{1450} = -23.0$ will have a negligible escape fraction of ionizing photons is quite unrealistic. Interestingly, Guaita et al. (2016) provided an example of an X-ray-selected AGN of $M_{1450} \sim -21.9$ at $z \sim 3.5$ with an escape fraction of 72% and other AGNs with lower values. If confirmed by more extended samples, it can indicate that fainter AGNs also can have a nonnegligible escape fraction of ionizing photons.

We can conclude from this analysis that the uncertainties in the escape fraction of the faint AGN population can give a maximum uncertainty of a factor of 2, with a photoionization rate that can be 2 times lower than our value provided in Table 4. This value has been derived by adopting a mean free path of 41.3 pMpc by Worseck et al. (2014). If we instead adopt a mean free path from Romano et al. (2019), which is ~ 1.3 times larger, then the resulting photoionization rate would be even higher. In practice, the uncertainties in the escape fraction and mean free path can compensate each other. In summary, the value of the photoionization rate provided in Table 4 is robust with respect to the uncertainties in the physical properties of the faint AGN population and the IGM.

At present, the measurement of the photoionizing background from the literature, based mainly on the Lyman forest fitting, is uncertain by a factor of 2 (Faucher-Giguère et al. 2008; Becker & Bolton 2013). Considering that our estimate of Γ is also uncertain by a factor of 2, it can be concluded that our result does not support a scenario where AGNs give a minor contribution to the ionizing UV background already at $z = 4$ as proposed by, for example, Kulkarni et al. (2019) and Kim et al. (2020). Thus, it would be safe to conclude that, modulo the present uncertainties in the escape fraction of faint AGNs and the mean free path at $z = 4$, the QSO/AGN population alone can provide the amount of radiation required to keep the cosmological hydrogen fully ionized at these redshifts.

6. Conclusions

From the QSO LF analysis at $z \sim 4$ and $-29.5 < M_{1450} < -28.0$ from the QUBRICS survey it is possible to draw the following conclusions:

1. Our $z \sim 4$ LF extends to an unprecedented absolute magnitude of $M_{1450} = -29.5$. This result confirms the uniqueness of the QUBRICS survey in finding the most luminous objects in the distant universe.
2. The best fit for the bright-end slope of the $z \sim 4$ LF is $\beta = -4.025$, significantly steeper than the slopes by Fan et al. (2001), Akiyama et al. (2018), Parsa et al. (2018), and Shen et al. (2020). The expected slope is in agreement with

- the ones found by Schindler et al. (2019a, 2019b) at similar redshifts. This implies that there is little evolution of the slope of the bright end of the QSO LF from $z = 1$ to $z = 4$.
3. We find a higher space density of bright QSOs at $z \sim 4$ with respect to SDSS by a factor of 30%–40%, confirming previous results by Schindler et al. (2019a, 2019b).
4. Our observed best-fit QSO LF at $z \sim 4$ is in tension with the results previously obtained by Fan et al. (2001), Akiyama et al. (2018), Parsa et al. (2018), Kulkarni et al. (2019), and Shen et al. (2020). More specifically, at bright magnitudes, the space density calculated by our survey is higher than all previously presented fits. Also at fainter magnitudes, most previous surveys failed to reproduce the observed data points by F07 and Boutsia et al. (2018), leading to underestimating the faint-end slope.
5. The H I ionizing background produced by bright QSOs and faint AGNs (up to $M_{1450} = -18$) is $\text{Log}(\Gamma [s^{-1}]) = -12.17^{+0.13}_{-0.07}$ (at the 3σ confidence level), which is close to the value measured by Becker & Bolton (2013) at similar redshifts. Our value has been derived by assuming a LyC escape fraction of 0.7 for the whole QSO and AGN population (Grazian et al. 2018) and a mean free path of 41.3 pMpc (Worseck et al. 2014). If the mean free path calculated by Romano et al. (2019) is instead adopted, the photoionization rate produced by AGNs can be higher by a factor of ~ 1.3 .

The comparison of our observed QSO LF at $z \sim 4$ with the predictions of two SAMs shows that the extremely bright end probed by QUBRICS could give critical insights into the recipes for triggering QSO activity in massive dark matter halos. In the future, it is important to extend the QUBRICS survey to deeper regions of the sky in order to robustly determine the location of the break and the faint-end slope of the QSO LF at $z \sim 4$ and beyond, with a survey as complete as possible. This attempt will require a large investment of telescope time, but it will be feasible in the near future thanks to the large imaging databases of the Vera Rubin telescope (LSST), the large field of view of the Roman Space Telescope (former WFIRST), and the powerful spectroscopic capabilities of wide-field spectrographs planned in the next decades.

A.G. and F.F. acknowledge support from PRIN MIUR project “Black Hole winds and the Baryon Life Cycle of Galaxies: the stone-guest at the galaxy evolution supper,” contract 2017-PH3WAT.

This work has made use of data from the European Space Agency (ESA) mission Gaia (<https://www.cosmos.esa.int/gaia>), processed by the Gaia Data Processing and Analysis Consortium (DPAC, <https://www.cosmos.esa.int/web/gaia/dpac/consortium>). Funding for the DPAC has been provided by national institutions, in particular the institutions participating in the Gaia Multilateral Agreement.

This paper includes data gathered with the 6.5 m Magellan Telescopes located at Las Campanas Observatory (LCO), Chile.

The national facility capability for SkyMapper has been funded through ARC LIEF grant LE130100104 from the Australian Research Council, awarded to the University of Sydney, the Australian National University, Swinburne University of Technology, the University of Queensland, the University of Western Australia, the University of Melbourne, Curtin University of Technology, Monash University. and the

Australian Astronomical Observatory. SkyMapper is owned and operated by the Australian National University's Research School of Astronomy and Astrophysics. The survey data were processed and provided by the SkyMapper Team at the Australian National University. The SkyMapper node of the All-Sky Virtual Observatory (ASVO) is hosted at the National Computational Infrastructure (NCI). Development and support of the SkyMapper node of the ASVO has been funded in part by Astronomy Australia Limited (AAL) and the Australian Government through the Commonwealth's Education Investment Fund (EIF) and National Collaborative Research Infrastructure Strategy (NCRIS), particularly the National eResearch Collaboration Tools and Resources (NeCTAR) and the Australian National Data Service Projects (ANDS).

This publication makes use of data products from the Wide-field Infrared Survey Explorer, which is a joint project of the University of California, Los Angeles, and the Jet Propulsion Laboratory/California Institute of Technology, funded by the National Aeronautics and Space Administration.


Facilities: Skymapper, Wise, Gaia, Magellan:Baade (IMACS), Magellan:Clay (LDSS-3).

ORCID iDs

Konstantina Boutsia  <https://orcid.org/0000-0003-4432-5037>

Andrea Grazian  <https://orcid.org/0000-0002-5688-0663>

Fabio Fontanot  <https://orcid.org/0000-0003-4744-0188>

Emanuele Giallongo  <https://orcid.org/0000-0003-0734-1273>

Nicola Menci  <https://orcid.org/0000-0002-4096-2680>

Giorgio Calderone  <https://orcid.org/0000-0002-7738-5389>

Stefano Cristiani  <https://orcid.org/0000-0002-2115-5234>

Valentina D'Odorico  <https://orcid.org/0000-0003-3693-3091>

Guido Cupani  <https://orcid.org/0000-0002-6830-9093>

Francesco Guarneri  <https://orcid.org/0000-0003-4740-9762>

References

- Akiyama, M., He, W., Ikeda, H., et al. 2018, *PASJ*, 70, S34
- Anderson, T. 2003, *An Introduction to Multivariate Statistical Analysis* (3rd edn.; New York: Wiley)
- Bañados, E., Venemans, B. P., Mazzucchelli, C., et al. 2018, *Natur*, 553, 473
- Becker, G. D., & Bolton, J. S. 2013, *MNRAS*, 436, 1023
- Boutsia, K., Grazian, A., Calderone, G., et al. 2020, *ApJS*, 250, 26
- Boutsia, K., Grazian, A., Giallongo, E., Fiore, F., & Civano, F. 2018, *ApJ*, 869, 20
- Boyle, B. J., Griffiths, R. E., Shanks, T., Stewart, G. C., & Georgantopoulos, I. 1993, *MNRAS*, 260, 49
- Calderone, G., Boutsia, K., Cristiani, S., et al. 2019, *ApJ*, 887, 268
- Chambers, K. C., Magnier, E. A., Metcalfe, N., et al. 2016, arXiv:1612.05560
- Cristiani, S., Serrano, L. M., Fontanot, F., Vanzella, E., & Monaco, P. 2016, *MNRAS*, 462, 2478
- D'Aloisio, A., McQuinn, M., Davies, F. B., & Furlanetto, S. R. 2018, *MNRAS*, 473, 560
- Dayal, P., Volonteri, M., Choudhury, T. R., et al. 2020, *MNRAS*, 495, 3065
- Eales, S. 1993, *ApJ*, 404, 51
- Fan, X., Carilli, C. L., & Keating, B. 2006, *ARA&A*, 44, 415
- Fan, X. & SDSS Collaboration 2000, AAS Meeting Abstracts, 197, 27.01
- Fan, X., Strauss, M. A., Schneider, D. P., et al. 2001, *AJ*, 121, 54
- Faucher-Giguère, C.-A., Lidz, A., Hernquist, L., & Zaldarriaga, M. 2008, *ApJ*, 688, 85
- Fiore, F., Feruglio, C., Shankar, F., et al. 2017, *A&A*, 601, A143
- Fontanot, F., Cristiani, S., Monaco, P., et al. 2007, *A&A*, 461, 39
- Fontanot, F., Cristiani, S., Pfrommer, C., Cupani, G., & Vanzella, E. 2014, *MNRAS*, 438, 2097
- Fontanot, F., De Lucia, G., Hirschmann, M., et al. 2020, *MNRAS*, 496, 3943
- Gaia Collaboration, Brown, A. G. A., Vallenari, A., et al. 2018, *A&A*, 616, A1
- Gaia Collaboration, Brown, A. G. A., Vallenari, A., et al. 2021, *A&A*, 649, A1
- Gehrels, N. 1986, *ApJ*, 303, 336
- Giallongo, E., Grazian, A., Fiore, F., et al. 2015, *A&A*, 578, A83
- Giallongo, E., Grazian, A., Fiore, F., et al. 2019, *ApJ*, 884, 19
- Glikman, E., Djorgovski, S. G., Stern, D., et al. 2011, *ApJL*, 728, L26
- Grazian, A., Giallongo, E., Boutsia, K., et al. 2018, *A&A*, 613, A44
- Gregg, M. D., Becker, R. H., White, R. L., et al. 1996, *AJ*, 112, 407
- Guita, L., Pentericci, L., Grazian, A., et al. 2016, *A&A*, 587, A133
- Haardt, F., & Madau, P. 2012, *ApJ*, 746, 125
- Hopkins, P. F., Richards, G. T., & Hernquist, L. 2007, *ApJ*, 654, 731
- Jiang, L., McGreer, I. D., Fan, X., et al. 2016, *ApJ*, 833, 222
- Kim, Y., Im, M., Jeon, Y., et al. 2020, *ApJ*, 904, 111
- Koo, D. C., & Kron, R. G. 1988, *ApJ*, 325, 92
- Kulkarni, G., Worseck, G., & Hennawi, J. F. 2019, *MNRAS*, 488, 1035
- Lyke, B. W., Higley, A. N., McLane, J. N., et al. 2020, *ApJS*, 250, 8
- Marshall, H. L., Tananbaum, H., Avni, Y., & Zamorani, G. 1983, *ApJ*, 269, 35
- Matsuoka, Y., Iwasawa, K., Onoue, M., et al. 2019, *ApJ*, 883, 183
- McGreer, I. D., Jiang, L., Fan, X., et al. 2013, *ApJ*, 768, 105
- Menci, N., Gatti, M., Fiore, F., & Lamastra, A. 2014, *A&A*, 569, A37
- Mitchell, P. S., Miller, L., & Boyle, B. J. 1990, *MNRAS*, 244, 1
- Morishita, T., Stiavelli, M., Trenti, M., et al. 2020, *ApJ*, 904, 50
- Pâris, I., Petitjean, P., Aubourg, É., et al. 2018, *A&A*, 613, A51
- Parsa, S., Dunlop, J. S., & McLure, R. J. 2018, *MNRAS*, 474, 2904
- Peterson, B. A., Savage, A., Jauncey, D. L., & Wright, A. E. 1982, *ApJL*, 260, L27
- Prochaska, J. X., Worseck, G., & O'Meara, J. M. 2009, *ApJL*, 705, L113
- Richards, G. T., Hall, P. B., Vand en Berk, D. E., et al. 2003, *AJ*, 126, 1131
- Romano, M., Grazian, A., Giallongo, E., et al. 2019, *A&A*, 632, A45
- Sargent, W. L. W., Steidel, C. C., & Boksenberg, A. 1989, *ApJS*, 69, 703
- Schindler, J.-T., Fan, X., Huang, Y.-H., et al. 2019a, *ApJS*, 243, 5
- Schindler, J.-T., Fan, X., McGreer, I. D., et al. 2017, *ApJ*, 851, 13
- Schindler, J.-T., Fan, X., McGreer, I. D., et al. 2019b, *ApJ*, 871, 258
- Schmidt, M., & Green, R. F. 1983, *ApJ*, 269, 352
- Schneider, D. P., Hall, P. B., Richards, G. T., et al. 2005, *AJ*, 130, 367
- Shen, X., Hopkins, P. F., Faucher-Giguère, C.-A., et al. 2020, *MNRAS*, 495, 3252
- Skrutskie, M. F., Cutri, R. M., Stiening, R., et al. 2006, *AJ*, 131, 1163
- Springel, V., White, S. D. M., Jenkins, A., et al. 2005, *Natur*, 435, 629
- Storrie-Lombardi, L. J., McMahon, R. G., Irwin, M. J., & Hazard, C. 1996, *ApJ*, 468, 121
- Travascio, A., Zappacosta, L., Cantalupo, S., et al. 2020, *A&A*, 635, A157
- Trump, J. R., Hall, P. B., Reichard, T. A., et al. 2006, *ApJS*, 165, 1
- Ueda, Y., Akiyama, M., Hasinger, G., Miyaji, T., & Watson, M. G. 2014, *ApJ*, 786, 104
- Volonteri, M., Pfister, H., Beckmann, R. S., et al. 2020, *MNRAS*, 498, 2219
- Wang, F., Yang, J., Fan, X., et al. 2018, *ApJL*, 869, L9
- Wolf, C., Onken, C. A., Luvaul, L. C., et al. 2018, *PASA*, 35, e010
- Worseck, G., Davies, F. B., Hennawi, J. F., & Prochaska, J. X. 2019, *ApJ*, 875, 111
- Worseck, G., Prochaska, J. X., O'Meara, J. M., et al. 2014, *MNRAS*, 445, 1745
- Wright, E. L., Eisenhardt, P. R. M., Mainzer, A. K., et al. 2010, *AJ*, 140, 1868
- Wyithe, J. S. B., & Bolton, J. S. 2011, *MNRAS*, 412, 1926
- Yang, J., Wang, F., Fan, X., et al. 2019, *AJ*, 157, 236
- Yang, J., Wang, F., Fan, X., et al. 2020, *ApJL*, 897, L14